Cold Regions Science and Technology 216 (2023) 104008

Contents lists available at ScienceDirect

Cold Regions Science and Technology

journal homepage: www.elsevier.com/locate/coldregions

Glaciological and meteorological investigations of an Alpine debris-covered glacier: the case study of Amola Glacier (Italy)

Davide Fugazza [a,*], Barbara Valle [b], Marco Stefano Caccianiga [c], Mauro Gobbi [d], Giacomo Traversa [e], Marta Tognetti [f], Guglielmina Adele Diolaiuti [a], Antonella Senese [a]

[a] Department of Environmental Science and Policy, Università degli Studi di Milano, 20133 Milan, Italy
[b] Department of Life Sciences, University of Siena, 53100 Siena, Italy
[c] Department of Biosciences, Università degli Studi di Milano, 20133 Milan, Italy
[d] Research and Museum Collections Office, Climate and Ecology Unit, MUSE-Science Museum, 38122 Trento, Italy
[e] Institute of Polar Sciences, National Research Council (CNR-ISP), 20126 Milan, Italy
[f] Giardino botanico Alpino Rezia, 23032 Bormio, SO, Italy

ARTICLE INFO

Keywords:
Debris-covered glacier
Landsat 8 TIRS
Melt model
Adamello-Presanella Massif

ABSTRACT

Debris-covered glaciers are common in many regions of the world, and accurately modelling their melt is of increasing importance for water resources planning, and biological and ecological research. In this study, we investigate meteorological and glaciological conditions and estimate the melt of Amola Glacier (a small debris-covered glacier in the Adamello-Presanella Massif, Italian Alps) using an empirical approach, based on shortwave radiation, surface temperature, debris thickness and thermal resistance. Meteorological conditions are determined from a supraglacial automatic weather station, while the model is calibrated using i) field data acquired during the ablation season 2020, including a network of ablation stakes and thermistors, ii) modelled solar radiation and iii) thermal imagery from Landsat 8 TIRS.

The analysis of glacier meteorological conditions shows a high prevalence of cloud-covered (50.60% of daytime observations) and humid conditions, with a high daily air temperature range (22.24 °C). Analysis of thermistor data suggests that a linear thermal gradient of the debris layer can be assumed when the model is run at daily resolution. Modelled debris thickness, surface temperatures and melt capture patterns observed on the field, including the decrease in debris thickness and increasing melt with elevation and their variability across the glacier surface. The root mean square error between measured and observed melt is 0.16 m, corresponding to 22% of the average observed melt, in line with the performance of empirical models for debris-free and debris-covered ice. The model could thus be used to provide a first estimate of debris-covered ice melt for glaciers in the Adamello region. Improvements to the model would require measuring all energy fluxes on the glacier from a weather station and investigating their spatial distribution on the glacier surface.

Abbreviations: SWin, incoming shortwave radiation (W m^{-2}); SWout, outgoing shortwave radiation flux (W m^{-2}); LWin, incoming longwave radiation (W m^{-2}); LWout, outgoing longwave radiation (W m^{-2}); T, air temperature (°C); RH, relative humidity (%); DT, debris thickness (m); T_s, debris surface temperature (°C); $SWin_{CS}$, incoming shortwave radiation during clear sky conditions (W m^{-2}); τ, atmospheric transmissivity depending on cloud cover; $SWin_{Amola}$, incoming solar radiation measured by AWS_{Amola} in real atmospheric conditions (W m^{-2}); I_0, average solar irradiance at the mean Earth-Sun distance (1367 W m^{-2}); E_0, eccentricity factor; k, factor used to express SWin in the correct measure unit; δ, solar declination; Φ, latitude; S, slope of the grid cell; w_{sr} and w_{ss}, sunrise and sunset hour angles, respectively; A, aspect of the grid cell; $SWin_{Caret}$, incoming solar radiation measured by the station located at Malga Caret (W m^{-2}); $SWin_{Pinzolo}$, incoming solar radiation measured by the station located at Pinzolo (W m^{-2}); $SWin_{Cima\ Presena}$, incoming solar radiation measured by the station located at Cima Presena (W m^{-2}); σ, Stefan-Boltzmann constant (5.67 × 10^{-8} W m^{-2} K^{-4}); M, amount of ice melt under a debris cover (m of surface lowering); T_i, temperature at debris-ice interface (°C); Δt, time step; ρ_i, ice density (917 kg m^{-3}); DR, effective thermal resistance of the debris layer (m^2 °C W^{-1}); L_m, latent heat of melting (3.34 × 10^5 J kg^{-1}).

* Corresponding author.
E-mail address: davide.fugazza@unimi.it (D. Fugazza).

https://doi.org/10.1016/j.coldregions.2023.104008
Received 12 October 2022; Received in revised form 26 June 2023; Accepted 8 September 2023
Available online 9 September 2023

1. Introduction

During the current phase of global warming, alpine glaciers are exhibiting two major trends: a general mass loss, due to cumulated negative mass balances (Marzeion et al., 2017; Roe et al., 2017) and an increase of thin debris cover on the ice surface due to englacial melt-out (Anderson and Anderson, 2016; Kirkbride and Deline, 2013), and an intensification of cryo- and thermo- clastism (Azzoni et al., 2018; Paul et al., 2007). Beside the Alps, the increase in debris-covered area has been reported for glaciers of all middle and low latitudes (Benn et al., 2014; Bocchiola et al., 2018; Kirkbride, 2011; Mihalcea et al., 2008b; Mihalcea et al., 2008a; Soncini et al., 2015).

When this debris cover is consistent and mantles most of the ablation area, the glacier can be considered a debris-covered glacier (Benn and Evans, 2010). When the debris exceeds a "critical thickness" (sensu Mattson et al., 1993), it slows glacier recession since the debris cover causes a logarithmic reduction of the ablation rate and, consequently, of the frontal variations (Belloni and Pelfini, 1995; Nakawo and Rana, 1999; Østrem, 1959). This allows glaciers to reach lower elevation such as Miage and Belvedere Glaciers (Italian Alps) where the terminus is at an elevation lower than the treeline (Tampucci et al., 2016). However, local areas of high melt also develop at supraglacial ponds and exposed ice cliffs, and thus mass losses are often similar for debris-covered and debris-free glaciers (Stefaniak et al., 2021).

The cryosphere is an important source of freshwater (Huss et al., 2017) that regulates the hydrological cycle of Alpine basins and influences the development of alpine ecosystems (Barnett et al., 2005; Beniston et al., 2003; Chesnokova et al., 2020; Huss and Hock, 2018). In some mountain ranges such as the Karakoram, large debris-covered glaciers are prevalent, and their meltwater is crucial for industrial and domestic use (Kraaijenbrink et al., 2017; Senese et al., 2018a). Moreover, the glacier surface represents a favourable habitat for a large number of species (e.g. from bacteria, Franzetti et al., 2017; to arthropods, Valle et al., 2022, and plants, Caccianiga et al., 2011), and there is evidence that over the past decades a number of threatened high elevation and cold-adapted species have taken refuge on debris-covered glaciers in response to climate change (Tampucci et al., 2017), highlighting the great ecological and biogeographic importance of this peculiar habitat for high elevation biodiversity. For these reasons, the study of debris-covered glaciers is becoming crucial in order to predict the evolution of the cryosphere and its consequences on the biosphere.

Unlike for debris-free glaciers, modelling melt of buried ice requires more information and assumptions since the presence of debris modulates the melting of the covered ice; while progress has been made towards more accurate models since the first studies of debris covered ice melt (Nakawo and Rana, 1999; Nakawo and Young, 1981), several sources of uncertainty still exist, particularly with respect to the energy fluxes and thermal conditions of the surface. In fact, accurate knowledge of the properties of the debris layer is necessary in order to better quantify the energy available for melt at the debris-ice interface, including the thickness of the layer, its thermal conductivity and the temperature of the debris at the surface (Gibson et al., 2018). As surface temperature is generally difficult to accurately obtain across spatial and temporal scales, in some studies it is derived numerically from the inversion of the energy balance equation. For example, Nicholson and Benn (2006) applied a modified surface energy balance model to calculate melt beneath a debris layer from daily mean meteorological data; such an approach was further refined by Reid and Brock (2010) and Rounce et al. (2015), among others. These methods require the deployment of an automatic weather station on the glacier surface carrying all the necessary instruments to derive the energy fluxes, which is not always practical or possible on a glacier. Besides, as thermal conductivity is also influenced by the debris porosity (depending on grain size distribution), lithology and humidity (Mattson et al., 1993), extensive field data are required to determine these variables.

Thus, in other studies a simplified approach was proposed based on the computation of the conductive heat flux through the debris layer (Han et al., 2006), where surface temperature is derived empirically. Distributing the debris thickness of the glacier is also complicated and most approaches estimate it through satellite thermal data (e.g. Fujita and Sakai, 2014; Minora et al., 2015; Senese et al., 2018a; Zhang et al., 2011).

In this study, we used the empirical approach (see also Mihalcea et al., 2008a, 2008b; Minora et al., 2015) which requires knowledge of patterns of incoming shortwave radiation, debris thickness, and surface temperature and thermal resistance of the debris layer. Our aims are:

1) To define meteorological and glaciological conditions on Amola glacier.
2) To model the melt of the debris-covered portions of Amola glacier using an empirical model driven mainly by surface temperature and thermal resistance of the debris layer.

2. Study area

The study was performed on the Amola glacier (Eastern Italian Alps: 46°13′10.1″N 10°41′08.7″E, Fig. 1), a debris-covered glacier with an area of 0.68 km^2 (Paul et al., 2020) that is located in the Adamello-Presanella Massif within the protected area of the Adamello Natural Park (Baroni et al., 2004). The glacier covers the elevation range from approximately 2570 to 3150 m a.s.l. (Paul et al., 2020). Amola glacier has an Easterly aspect and is surrounded by the Presanella (3557 m a.s.l.) and other peaks constituted by tonalite, a rock of the diorite class characterised by lower thermal conductivity and higher reflectance than most metamorphic and sedimentary rocks (Bocchiola et al., 2015). Tonalite rocks cover almost the entire glacier ablation area (debris cover: 60%; 2020 satellite data), with a coarse grain size that ranges from a few millimetres to about 1 m (Gobbi et al., 2017).

Average annual precipitation in the area of the Park is about 1000 mm (Bocchiola and Diolaiuti, 2010). Several glaciers are hosted within the Park area, including the widest glacier of Italy, Adamello glacier (Maragno et al., 2009). Previous studies on Amola glacier have focused on the colonisation of supraglacial debris and the glacier foreland by ground-beetles, spiders and springtails (Gobbi et al., 2017; Tenan et al., 2016), on plant-insect interactions on the glacier and along the chronosequence of glacier retreat (Losapio et al., 2015) and a relatively uninterrupted series of terminus variations exists (Gobbi et al., 2017); however, detailed studies on thickness patterns of supraglacial debris and their influence on meltwater production are lacking for this glacier.

Amola Glacier was selected as it was the subject of several studies on communities of epiglacial plants and invertebrates (i.e. ERC project "Ice Communities - Reconstructing community dynamics and ecosystem functioning after glacial retreat", BIODIVERSA+ PrioritICE project "Vanishing habitats: conservation priorities for glacier-related biodiversity threatened by climate change"). In addition, it was the selected study area for the PhD project "Plant and arthropod communities of Alpine ice-related landforms: ecological and biogeographic importance" (at the University of Milan). Amola Glacier was also selected for long-term interdisciplinary studies related to epiglacial biodiversity and the environmental factors that limit its survival. Moreover, it can be considered representative of Italian debris-covered glaciers for its size. The New Italian Glacier Inventory (Smiraglia et al., 2015), lists 903 glaciers in Italy, of which 114 are considered debris-covered (13%). These cover on average an area of 0.40 km^2 ranging from 0.01 km^2 (relative to 7 glacierets) to 10.47 km^2 of Miage Glacier. 108 glaciers (95%) have an area lower than 0.80 km^2. In this inventory, Amola Glacier had in 2011 an area of 0.78 km^2.

3. Data and methods

In this study, we used data from a supraglacial Automatic Weather Station (AWS) to define the glacier meteorological conditions and

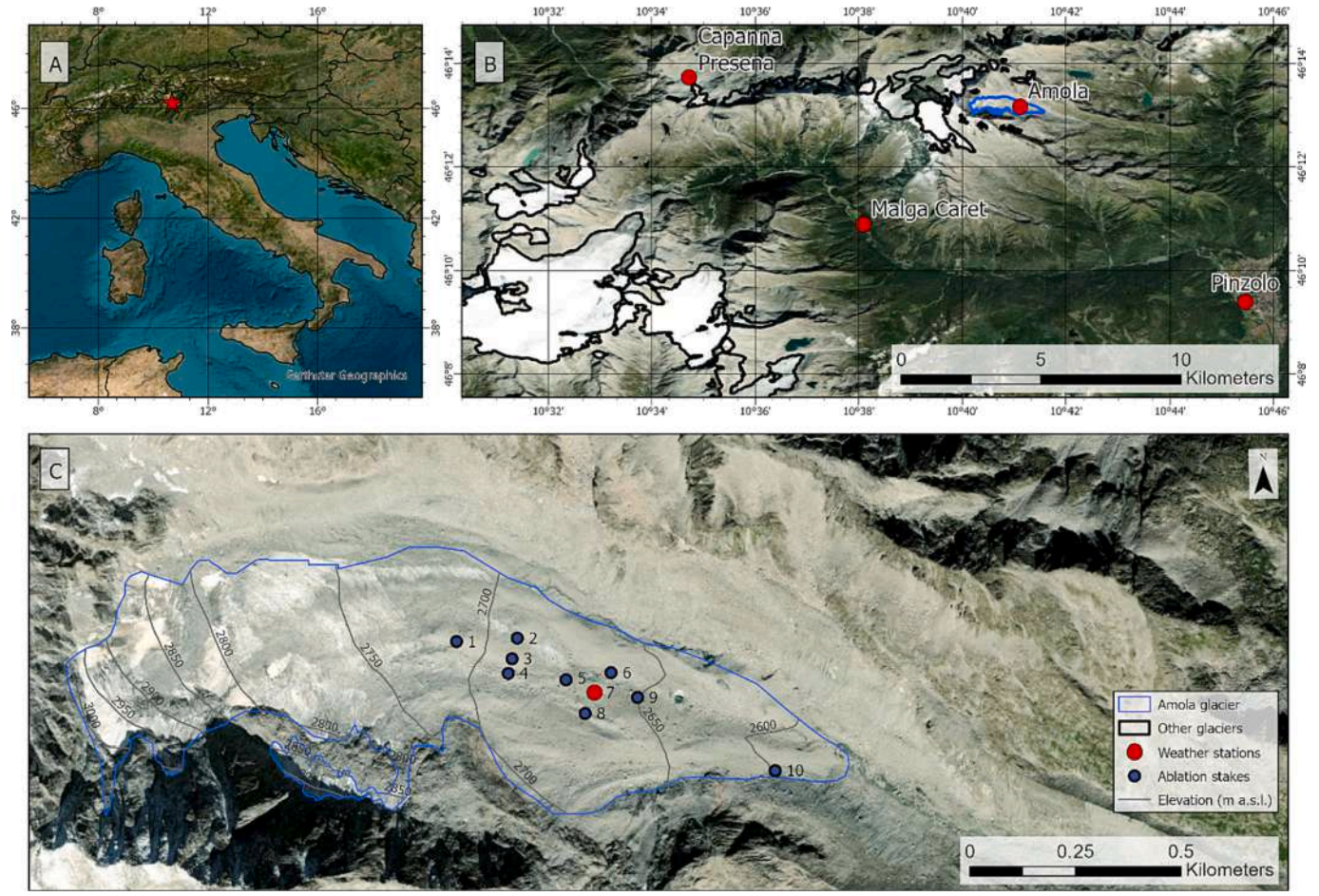

Fig. 1. Location of Amola glacier within Italy (A) and Adamello Massif, with weather stations from MeteoTrentino (B). High resolution image of Amola glacier (C) with contour lines, location of ablation stakes and the automatic weather station (corresponding to number 7) (bottom). Basemap from Bing aerial maps©.

particularly incoming shortwave radiation. Coupled with ice melt under the debris layer measured through ablation stakes, measurements of debris thickness and debris surface temperature from thermistors placed over debris of varying thickness and a Landsat 8 satellite image, these data allowed us to model sub-debris ice melt. Additionally, we performed sensitivity tests, by i) using off-glacier AWSs to model incoming shortwave radiation and observe its impact on modelling sub-debris ice melt, and ii) comparing debris thickness maps obtained from different satellite images and observing their effect on modelling sub-debris ice melt.

3.1. Data

3.1.1. The automatic weather station AWS_{amola} and the observed meteorological data

An automatic weather station (AWS_{Amola}) was installed on 20 July 2020 on the debris-covered surface of the Amola Glacier (coordinates 46° 13′ 09.9" N and 10° 41′ 07.2″ E, at 2689 m a.s.l., position number 7 in Fig. 1, Fig. 2 for details); it was then removed on 18th August 2020. The station was equipped with a four-component radiometer (CNR4, Kipp&Zonen, with an accuracy of ±5%), a naturally ventilated thermo-hygrometer (HygroVUE10, Campbell Scientific, with an accuracy of ±0.1 °C for temperature measurements and ± 2% for relative humidity), and a low power data logger (PCTDA041, MTX, with a 4 Gb SD card, 3.6 V NiMH batteries and integrated 1 W solar panel); all instruments were mounted on a stainless steel tripod (AL300BA, MTX). Measurements of incoming and outgoing shortwave radiation (SWin and SWout), incoming and outgoing longwave radiation (LWin and LWout), air temperature (T) and relative humidity (RH) were sampled at 60-s intervals and minimum, mean and maximum values were recorded over a 30-min time period. We used all meteorological data for assessing the micro-meteorological conditions of the glacier, while only SWin was used to quantify buried ice melt.

The dataset was mostly uninterrupted, with gaps ranging from 27.6% to 31.5% of the total period depending on the parameter. Most of the gaps were due to a gradual nighttime depletion of the batteries and therefore they occurred generally in the early hours of the day.

3.1.2. Measurements of ablation, supraglacial debris temperature and thickness

Nine 2 m long ablation stakes made out of bamboo were drilled into the ice with a manual auger to evaluate ice melt under different conditions of debris thickness (according to the method introduced by Kaser et al., 2003). The stakes were placed on a longitudinal transect along the glacier centerline with two transverse intersecting transects (see numbers from 1 to 6 and from 8 to 10 in Fig. 1) and ice melt from 21 July 2020 to 18 August 2020 was measured. Except for stake 9, which was drilled in bare ice, all stakes were installed over a debris-covered surface. Debris thickness (DT) was measured in correspondence of each ablation stake and at the AWS_{Amola} in July; the debris was manually excavated before inserting the stake and care was taken to maintain the same thickness and stratigraphy after drilling. DT was also measured in August, and for some stakes differences were found between July and August observations owing to the movement of the glacier and possibly manual excavation and refilling of the layer; we therefore calculated the average of the two observations when this occurred.

Fig. 2. The weather station on Amola glacier AWS_{Amola}. Typical clast size of supraglacial debris is also shown.

Additionally, we measured debris surface temperature (T_s), which is a key element in calculating the energy available for melting of debris-covered ice, by means of Gemini Tinytag Plus thermistors (models TGP-4020, TGP-4500, TGP-4520 with a stated accuracy of 0.35 °C, 0.40 °C, 0.35 °C at 20 °C, respectively) at the location of the ablation stakes (except for stake 9 that was on bare ice). Each sensor probe was fixed with duct tape under a flat stone (2 cm thick) with a diameter of about 10 cm close to the stake in order to protect it from direct solar radiation, following Brock et al. (2010); the stone was then placed on the debris surface. The data recorded at this depth (2 cm) are normally considered indicative of point surface temperature, and used within several international protocols to study permafrost and frozen ground (see Guglielmin, 2006; Guglielmin et al., 2008; Osterkamp, 2003).In addition, at two sites (i.e. T8+ and T10) we measured the debris temperature at three different depths: surface (0.02 m), middle (0.10 m) and bottom (0.31 m and 0.20 m, respectively). Each data logger was programmed to acquire temperature readings every minute and record average measurements every 60 min. At stake 5 (see Fig. 1), the thermistor malfunctioned and it was therefore not possible to retrieve T_s; however, we placed an additional thermistor close to stake 8 (called T8+), and obtained a total dataset of 9 T_s records.

3.1.3. Satellite data

We downloaded a Landsat 8 OLI/TIRS image from 28 July 2020 from the Earth Explorer portal (https://earthexplorer.usgs.gov/) managed by the United States Geological Survey. The image was acquired at approximately 10 AM local time, and was downloaded from collection 1 level 1, which provides georeferenced and orthorectified images in the UTM projection; the image was selected to coincide in time with the period of observation of AWS_{Amola}, with no clouds covering the glacier and minimum snow cover.

Landsat 8 features 4 bands in the visible part of the electromagnetic spectrum, 2 in the near infrared and 2 in the shortwave infrared, all at 30 m spatial resolution, plus one panchromatic band at 15 m spatial resolution and two thermal bands at 100 m spatial resolution (provided already resampled to 30 m), with a 12 bit quantization. Compared to previous sensors of the Landsat family and ASTER used in other studies (Mihalcea et al., 2008a, 2008b; Minora et al., 2015), the presence of two thermal bands on Landsat 8, centred at 10.90 μm and 12 μm, makes it possible to derive surface brightness temperature using a split-window approach (Rozenstein et al., 2014), which corrects for atmospheric absorption by water vapour by taking into account the different absorption features of the two thermal bands.

A second image from 14 September 2020 was also used for sensitivity analysis, as this image was acquired outside of the period of observation of AWS_{Amola}. The image was acquired around the same time as the one from 28 July 2020 and features the same characteristics.

3.2. Methods

3.2.1. Gap filling of missing data from AWSAmola

As reported above, the AWS_{Amola} dataset was mostly uninterrupted, but some gaps occur especially during nighttime. During this period, SWin is null and therefore fortunately data gaps can be easily filled by setting SWin to 0 W m^{-2}. For the rest of the day (i.e. outside nighttime), we derived missing values of SWin from clear-sky solar radiation ($SWin_{CS}$, i.e. without cloudiness) and the atmospheric transmissivity depending on the cloud cover (τ) following Senese et al. (2016). Cloud transmissivity ranges between 0 and 1 and it is a factor that reduces the potential SWin of a quantity, which depends on the amount and type of clouds (Zhang et al., 1996). In fact, clouds reduce the direct component of SWin and then diffuse radiation prevails: following Konzelmann and Ohmura (1995), in completely overcast conditions diffuse radiation is ~15% of the total amount of incoming solar radiation. A value of $\tau = 1$ corresponds to a clear sky with no clouds (i.e. SWin = $SWin_{CS}$), whereas $\tau = 0$ means that no shortwave radiation reaches the surface at all. However, an overcast sky usually has $\tau > 0$ (i.e. SWin << $SWin_{CS}$), with different values for different cloud types. We considered $SWin_{CS}$ as the half-hourly solar radiation (W m^{-2}) for clear sky, assumed to be higher than the incoming radiation with clouds. Thus, we estimated $SWin_{CS}$ by considering the half-hourly SWin values measured by AWS_{Amola} on all days, and calculating the maximum value for each half-hour. In this way, the half-hourly trend of a typical clear sky day was derived. While this clear-sky incoming solar radiation can in principle be overestimated owing to multiple reflections from snow-covered surrounding slopes, this does not affect our measurements, since we considered a period of the year outside the snow accumulation period (from October to May) and thus with the higher probability that the surface surrounding the glacier is snow-free (i.e. from 21 July to 18 August 2020).

Subsequently, we used $SWin_{CS}$ for calculating the half-hourly cloud transmissivity (Senese et al., 2020):

$$\tau = \frac{SWin_{Amola}}{SWin_{CS}} \quad (1)$$

where $SWin_{Amola}$ is the incoming solar radiation measured by the AWS_{Amola} in real atmospheric conditions. Compared to $SWin_{Amola}$, $SWin_{CS}$ does not take into account the reduction of solar radiation due to actual atmospheric conditions (e.g. clouds). We assumed that the conditions of the sky remain constant over short periods (a few hours). Thus, we calculated the missing SWin values by considering the τ value of the following or previous half-hour and inverting Eq. (1). The reflected solar radiation data were filled considering an albedo of 0.18, which is the average of noon raw observations. When calculating the average albedo, we omitted these gap-filled values.

Regarding data gaps of the other meteorological parameters, we chose not to perform gap filling and to consider the actual measured

value as these were not used in the ablation model but to define the micro-meteorological conditions.

3.2.2. Incoming solar radiation model

To distribute the incoming solar radiation (SWin) over the Amola Glacier surface, we applied the algorithms tested over another Italian glacier, Forni Glacier, by Senese et al. (2016). The CNR4 net radiometer installed at the AWS_{Amola} is of the same type as that running at the AWS of the Forni Glacier (Senese et al., 2018b), therefore providing homogeneity of the two datasets and thus the applicability of the same model. For each grid cell we modelled SWin considering astronomical and geographical factors:

$$SW_{0-point} = I_0 \bullet E_0 \bullet k \bullet [(sin\,\delta \bullet sin\,\Phi \bullet cos\,S) \bullet (w_{ss} - w_{sr}) - (sin\,\delta \bullet cos\,\Phi \bullet cos\,S \bullet cos\,A) \bullet (w_{ss} - w_{sr}) + (cos\,\delta \bullet cos\,\Phi \bullet cos\,S) \bullet (sin\,w_{ss} - sin\,w_{sr}) + (cos\,\delta \bullet sin\,\Phi \bullet sin\,S \bullet cos\,A) \bullet (sin\,w_{ss} - sin\,w_{sr}) - (cos\,\delta \bullet sin\,A \bullet sin\,S) \bullet (cos\,w_{ss} - cos\,w_{sr})] \quad (2)$$

where I_0 is the average solar irradiance at the mean Earth-Sun distance (equal to 1367 W m^{-2}), E_0 is the eccentricity factor, k is a factor used to express SWin in the correct measure unit, δ is the solar declination, Φ is the latitude, S is the slope of the grid cell, w_{sr} and w_{ss} are the sunrise and sunset hour angles, respectively, and A is the aspect of the grid cell. Moreover, we estimated shading due to surrounding orography and the atmospheric absorption taking into account actual meteorological conditions, using the procedure described in Senese et al. (2016).

Senese et al. (2016) validated the approach by comparing the modelled SWin against the one measured at 18 sites along the glacier tongue, during summer 2011 and 2012. The modelled values agreed well with observations with a correlation coefficient of 0.97 and a root mean square error of 0.095 MJ m^{-2}.

For the last step regarding the atmospheric absorption, we tested the performance of the model comparing SWin values measured by AWS_{Amola} ($SWin_{Amola}$) with the ones obtained using data acquired by different automatic weather stations off-glacier from 21 July 2020 to 18 August 2020. Firstly, we used half-hourly data from the stations located at Malga Caret (Val Genova, 46.1814° N, 10.6348° E, 1418 m a.s.l., data available from 06-10-2011, $SWin_{Caret}$), Pinzolo (46.1565° N, 10.7575° E, 760 m a.s.l., data available from 01-01-1921, $SWin_{Pinzolo}$) and Cima Presena (46.2200° N, 10.5835° E, 3015 m a.s.l., data available from 14-12-1994, $SWin_{Presena}$). These stations were chosen since they are the closest to the Amola Glacier at a distance of 5.9 km, 9 km and 8.3 km, respectively (Fig. 1). Data can be freely downloaded from the website of Meteotrentino (https://www.meteotrentino.it/#!/content?menuItemDesktop=111).

3.2.3. Debris thickness model

Previous studies have observed good correlations between temperature measured from satellites and thickness of supraglacial debris. Mihalcea et al. (2008a) used different linear relationships to estimate DT from satellite T_s by dividing the surface of Miage glacier (Italy) into elevation bands; conversely, on Baltoro glacier a single exponential relationship was found as the best fit by Mihalcea et al. (2008b) and by Minora et al. (2015). We calculated surface temperature using the Landsat 8 TIRS image from 28 July 2020, using SPT, a QGIS plugin, to perform the extraction using the split-window approach (Rozenstein et al., 2014). The relationship between Landsat derived T_s and DT was then estimated using all available DT observations at the ablation stake sites, except for DT observed at AWS_{Amola}, which was used for validation. Given the small elevation range of Amola glacier, we preferred to use a single relationship and not divide the glacier into elevation bands. An exponential relationship was found as the best fit (Eq. (3)), with an R^2 of 0.65:

$$DT = 0.221e^{0.297T_s} \quad (3)$$

3.2.4. Debris surface temperature model

At the AWS_{Amola}, we derived surface temperature (T_s) from the emitted longwave radiation (LWout) by means of Stefan-Boltzmann law:

$$T_s = \sqrt[4]{\frac{LWout}{\sigma}} \quad (4)$$

where σ is the Stefan-Boltzmann constant equal to 5.67 × 10^{-8} W m^{-2} K^{-4}.

Over the rest of the glacier surface, as we could not estimate T_s from the inversion of the energy balance equation, we derived it by empirical correlation with SWin and DT. The relationship between these variables was demonstrated before on debris-covered areas (e.g. Mihalcea et al., 2008b): higher radiation fluxes and thicker debris lead to higher surface temperatures. First, we used T_s from thermistors, modelled SWin and DT measured at the 8 sites for the entire period of measurements (from 21 July 2020 to 18 August 2020) to establish a linear regression, with an R^2 of 0.47 (see Eq. (5)):

$$T_s = 0.079\,DT + 0.038\,SWin \quad (5)$$

This equation was then applied to estimate daily T_s across the glacier surface by using daily modelled SWin (see Section 3.2.2) and DT (see Section 3.2.3). We further calculated cumulated T_s as the sum of daily modelled T_s across the study period.

3.2.5. Debris-covered ice melt model

According to Minora et al. (2015), the amount of ice melt under a debris cover (M, m of surface lowering) depends on the energy available at the debris–ice interface that can be estimated assuming a linear temperature gradient from the top of the debris layer (T_s) to the ice surface (T_i) for mean daily conditions (e.g. Nakawo and Young, 1981):

$$M = \frac{(T_S - T_i) \bullet \Delta t}{DR \bullet \rho_i \bullet L_m} \quad (6)$$

where Δt is the time step, ρ_i is the ice density, DR is the effective thermal resistance of the debris layer (m^2 °C W^{-1}) and Lm is the latent heat of melting (3.34 × 10^5 J kg^{-1}). We set the ice surface temperature to the melting point, 0 °C, neglecting refreezing phenomena, which generally do not occur during the main ablation season (Minora et al., 2015) and impurities in the ice. An ice density of 917 kg m^{-3} was used (Senese et al., 2018b).

The assumption of a linear temperature gradient along the debris cover is given by the fact that if the physical properties in the debris layer are constant with depth, the heat flux depends linearly on the surface temperature for steady-state conditions. The thermal resistance can be assumed constant over an ablation season as it mainly depends on debris thickness, which is generally considered stable over short periods (1–2 months, Fyffe et al., 2014). To derive DR for each grid cell, an empirical relationship was applied based on DT (Minora et al., 2015) measured at the ablation stakes, with a R^2 of 0.67:

$$DR = 0.0056\,DT + 0.0341 \quad (7)$$

To restrict the melt model to the debris covered portions, a normalised difference snow index (NDSI) mask was computed from Landsat 8 OLI bands, using a threshold of 0.3 to separate ice/snow from the debris covered parts (Gjermundsen et al., 2011).

4. Results

4.1. Meteorological conditions

The data collected by the AWS_{Amola} are summarized in Fig. 3. Half-hourly average values of air temperature and relative humidity,

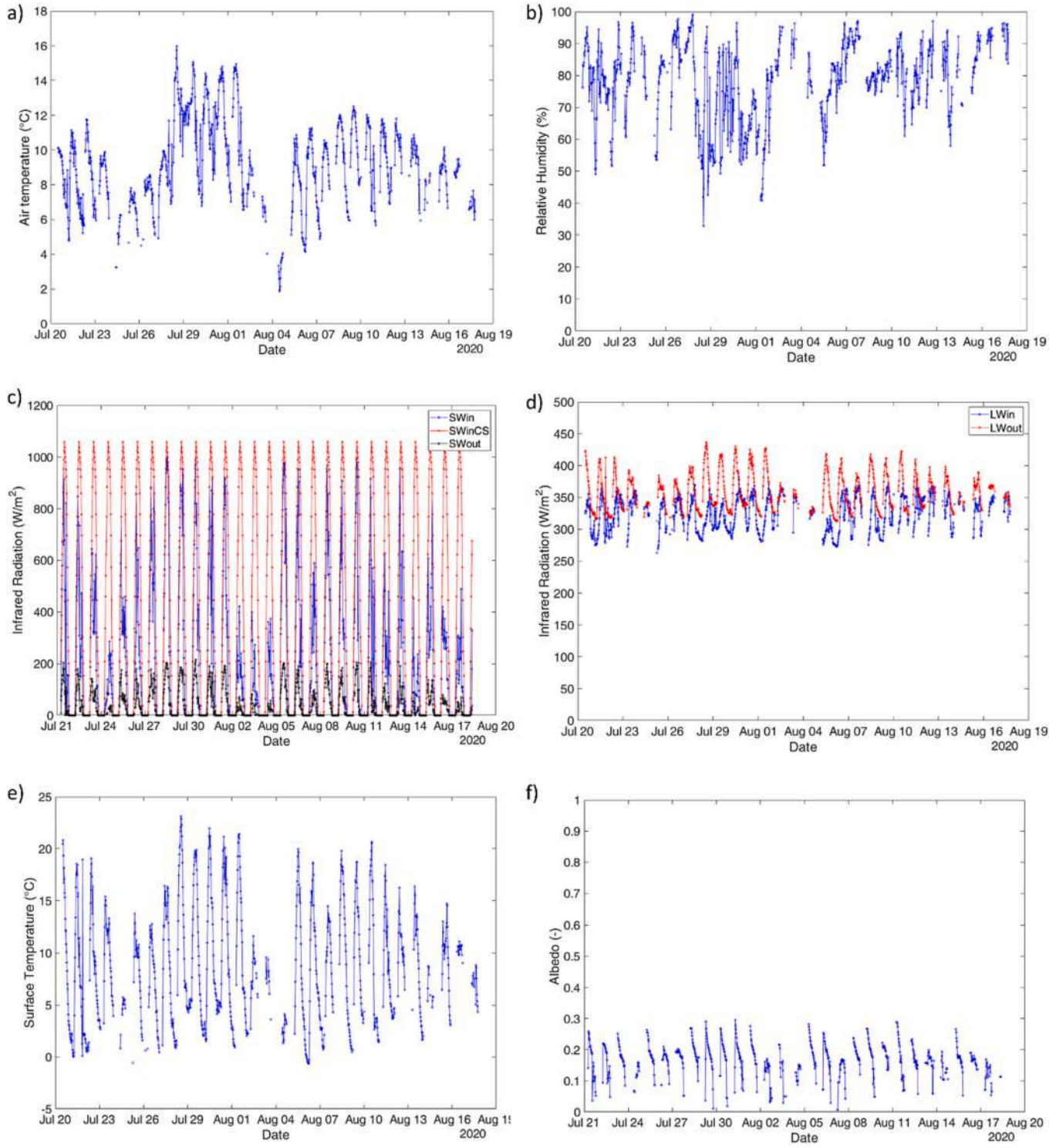

Fig. 3. Half-hourly average values of air temperature (A), relative humidity (B), incoming and reflected solar radiation (C), clear-sky solar radiation (C), incoming and emitted infrared radiation (D), surface temperature calculated from LWout (E) and albedo (F) are shown.

incoming and reflected solar radiation, clear-sky solar radiation, and incoming and outgoing infrared radiation are shown. The figure highlights the prevalence of data gaps during nighttime as reported in Section 3.2.1.

Air temperature ranges from +1.76 °C (recorded on 4 August at 12 PM) to +16.92 °C (recorded on 28 July at 1 PM) with a mean value of +9.24 °C (average of all half-hour mean values recorded by the instrument). Generally, minima occur during nighttime or just before dawn. The minimum value recorded by the AWS_{Amola} at 12 pm is due to very cold conditions that occurred during that day (Fig. 3a). The mean daily range is 5.66 °C, ranging from 2.00 °C (recorded on 16 August) to 10.39 °C (recorded on 28 July). Therefore, the warmest conditions and the widest amplitude occurred on 28 July. Most of the time (77.60%), half-hourly mean temperatures between +6 °C and + 12 °C prevail: 6–8 °C for 23.13%, 8–10 °C for 31.65% and 10–12 °C for 22.82% of the considered period.

The half-hourly air relative humidity ranges between 99.5% (recorded on 27 July at 8 PM) and 29.32% (recorded on 28 July at 12:30 PM

and 1 PM) with an average of 78.02% (Fig. 3b). Humid conditions prevail; in fact, there is only one occurrence of half-hourly relative humidity lower than 40%. Moreover, 76.66% of time relative humidity is higher than 70% and 50.26% of time > 80%.

As regards solar radiation (Fig. 3c), most of the considered period is found to be very cloudy since the clear sky index is lower than 0.40 for 50.60% of daytime observations (see Anslow et al., 2008). This high cloudiness can explain the data gaps, as the low wattage solar panel could not supply enough energy to the batteries during the day. Albedo is almost stable with a half-hourly mean value of 0.17 (Fig. 3f). The maximum is equal to 0.30 even if only 6.65% of half-hourly values are higher than 0.25; these high values are due to the normal daily cycle of albedo and values at early morning or late afternoon are not completely representative of the actual surface conditions (Azzoni et al., 2016). Considering daily values, the albedo ranges from 0.12 to 0.21 with a mean value of 0.18. Lower albedo values can be probably caused by rainy conditions or meltwater rising to the surface by capillarity, since a wet surface reflects less than a dry one (Hartmann, 2015).

The outgoing longwave radiation (Fig. 3d) and debris surface temperature (calculated applying Eq. (4), Fig. 3e) follow the daily thermal cycle of the air: higher values during daytime (maximum of 436.78 W m^{-2} corresponding to +23.11 °C recorded on 28 July at 1 PM) and lower ones during night time (minimum of 312.70 W m^{-2} corresponding to −0.64 °C recorded on 6 August at 5:30 AM). Despite an always positive air temperature, the debris surface also reaches negative values 1.05% of the time. The mean surface temperature is 8.73 °C. On a daily scale, only 2 days (25 July and 6 August) are characterised by freeze-thaw conditions (i.e. min < 0 °C and max >0 °C, Guglielmin et al., 2008). As regards thermal stress, the mean daily range is 13.42 °C and the maximum is 22.24 °C (on 28 July). These results suggest that supraglacial debris is more affected by thermoclastism and less by cryoclastism during the analysed period.

Moreover, from our findings, days with warmer air conditions occur with higher SWin fluxes (and higher τ) that heat the debris surface (i.e. higher T_s) which in turn emits more LWout that considerably affects air conditions with higher values of LWin.

4.2. Observed debris thickness and surface/subsurface temperatures

Debris thickness measured on the field from the average of July and August observations ranged between 0.05 m (at stake T3) and 0.32 m (at T8+); at most (7) sites however the thickness of the debris layer was lower than 0.10 m, and higher values were observed only at the terminus and other sites where local conditions favoured accumulation (e.g. at the base of lateral moraines).

Temperatures measured at the thermistor sites were rather homogeneous: for all thermistors except T8, the minimum temperature was recorded on the morning of 5 August, between 5 and 7 AM; the absolute minimum was −1.44 °C (T3, at 5 AM on 5 August). Daily maxima were recorded on 28 July at 3 PM for T2, T4, T6, T8, T10 and T8+, and the absolute maximum was +42.06 °C (T8+). Hourly T_s patterns are highly correlated, with a Pearson's correlation coefficient ranging between 0.77 (T3 and T10) and 0.99 (T2 and T6) (see Fig. S1).

Averaging T_s from thermistors to daily means, the minimum T_s was recorded on 4 August and the maximum on 28 July. The Pearson's correlation between the daily T_s from thermistors is even higher than for hourly values, ranging between 0.84 (T6 and T8) and 0.99 (T3 and T6), see Fig. 4.

Considering debris temperature at different depths from thermistors T8+ and T10, hourly temperatures show the dampening of daily temperature cycles with increasing depth, as the amplitude of the daily temperature range is reduced. At thermistor T8+, the average daily range is 6.29 °C at 0.31 m depth (close to the debris-ice interface) vs 24.81 °C at the surface, while at thermistor T10, it is 4.30 °C at 0.20 m depth and 9.66 °C at the surface. A lag of 1–2 h between debris temperature peaks and lows at different depths is also observed at both sites (see Fig. 5). While the behaviour of hourly debris temperatures is non-linear, the opposite is true for daily temperatures, especially at

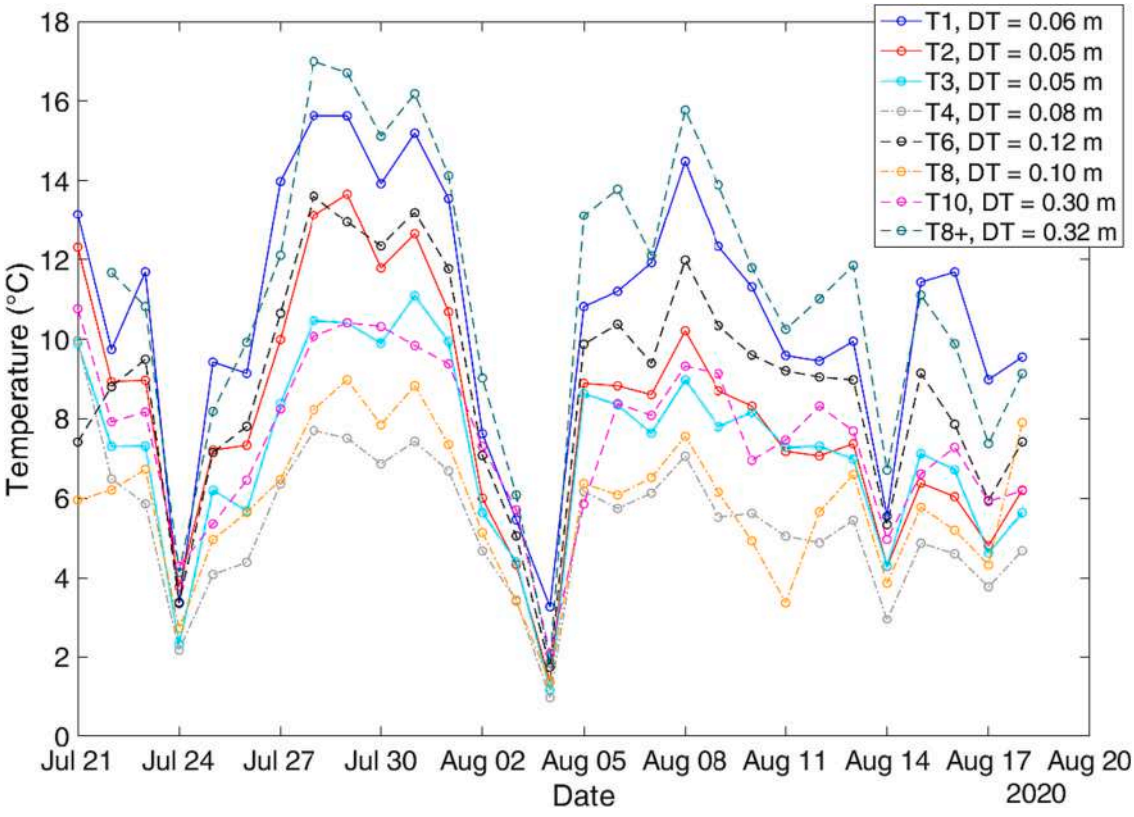

Fig. 4. Average daily debris surface temperature from thermistors located on Amola glacier. DT = debris thickness.

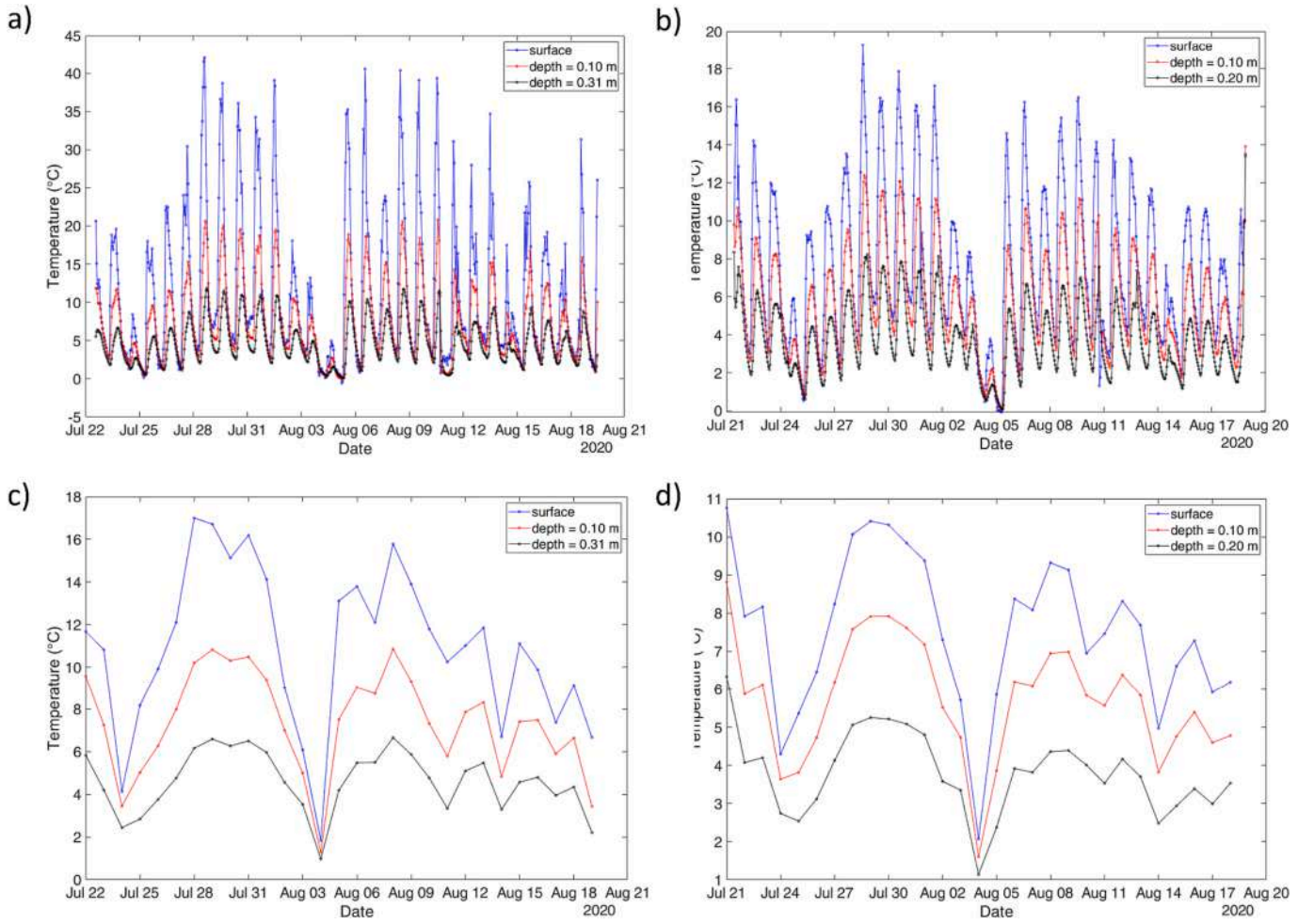

Fig. 5. Average hourly debris temperatures at different depths from thermistors T8+ and T10 (a and b, respectively); daily debris temperature at different depths from T8 and T10+ (c and c, respectively).

thermistor T10 (see Fig. 5). Considering a linear regression between temperature and depth, 15 out of 29 observations have a $R^2 > 0.85$ at T8+, while at T10 all observations have a $R^2 > 0.99$.

4.3. Modelled debris thickness, surface temperature and buried ice melt

From the NDSI mask based on the Landsat 8 OLI image, we calculated a debris-covered area of 0.40 km^2, corresponding to 59% of the Amola glacier surface. Debris is found up to 2760 m a.s.l., except for isolated patches at higher elevations, which might include dirty ice, with a temperature close to 0 °C (see Fig. 6a). The average modelled debris thickness is 0.08 m, with a maximum of 0.25 m, which in general slightly underestimates ground observations. Higher modelled DT is seen close to the terminus and the left flank of the glacier, while the lowest modelled values are seen above 2750 m a.s.l. (average DT < 0.01 m). Two patches with low modelled DT (0.03–0.05 m) are found in the middle of the debris-covered part, likely because the lateral rock walls are the main source of debris. Ground observations confirm the presence of patchy debris cover in these areas. At the AWS_{Amola}, (number 7 in Fig. 1) a DT of 0.08 m was modelled based on Landsat 8 TIRS, compared to an observed value of 0.05 m. Considering all DT measurements, we obtained a root mean square error (RMSE) of 0.03 m, a mean absolute error (MAE) of 0.02 m and a mean bias error (MBE) of 0.00 m from the comparison between measured and modelled values.

Cumulated modelled T_s follows the main pattern of debris cover, with a few differences (see Fig. 6b): a longitudinal band of lower modelled T_s along ice flow is seen at the terminus towards the hydrographic left part of the glacier, while on the hydrographic right flank higher modelled T_s occurs. This might be caused by the influence of solar radiation, as in those areas the topographic characteristics (slope and aspect) cause a different radiative input. The correlation between daily modelled T_s and observed T_s at thermistor T7, by the AWS_{Amola}, is 0.80; the RMSE between observed and modelled cumulated temperature is 62 °C, the bias is 3.62 °C and the MAE is 55 °C.

As regards glacier melt, the total modelled cumulated amount is 295 m^3; the average modelled total daily melt is 10.2 m^3 day^{-1} on the debris-covered part of the glacier or 0.03 m day^{-1} for each glacier cell. The highest total melt of >1.5 m between 21 July and 18 August 2020 is modelled at the upper reaches of debris cover (approximately 2760 m a.s.l.) while about 1 m is modelled in the lower central portion of the tongue, owing to the combined effect of low DT and higher cumulated temperatures (see Fig. 6c). Comparing modelled melt with observed melt at the stakes between 21 July 2020 and 18 August 2020, the maximum difference is found for stake 1, where modelled melt is 0.36 m higher than measured melt (35% of melt at the stake, see Table 1), while the minimum difference is 0.01 m for stake 10 and stake 7 (see Table 1), where AWS_{Amola} was located. Overall, the RMSE is 0.16 m, the bias is +0.03 m (modelled - measured) and the mean absolute error is 0.12 m, with a correlation coefficient of 0.50.

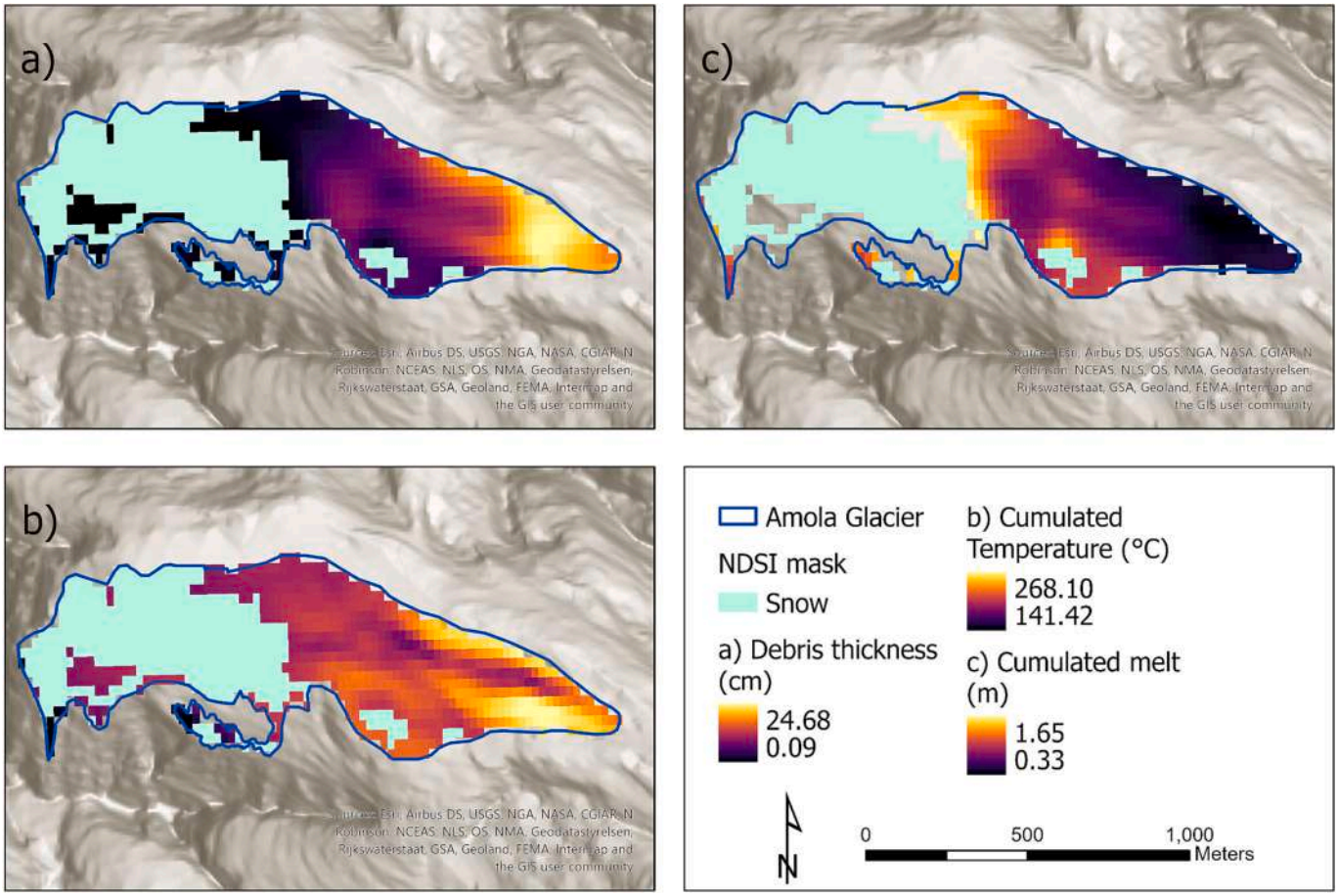

Fig. 6. a) Debris thickness distribution obtained from Landsat 8 TIRS acquired on 28 July 2020; b) Cumulated temperature from 21 July to 18 August 2020 from Eq. (5); c) Cumulated melt between 21 July and 18 August 2020.

Table 1
Comparison between cumulated measured and modelled melt at the stakes located on Amola glacier from 21 July to 18 August 2020.

Stake number	Measured melt (m)	Modelled melt (m)	Difference (m)
1	0.68	1.04	−0.36
2	0.73	0.81	−0.08
3	0.89	0.77	0.12
4	0.93	0.74	0.19
5	0.91	0.92	−0.01
6	0.66	0.60	−0.06
7	0.80	0.76	−0.04
8	0.50	0.73	−0.23
10	0.44	0.45	−0.01

5. Discussion

5.1. Using off- glacier weather stations to distribute incoming solar radiation

From the comparison between $SWin_{Amola}$ and the modelled values $SWin_{Caret}$, $SWin_{Pinzolo}$ and $SWin_{Presena}$ (Fig. 7), we found errors ranging from 153.46 W m^{-2} (84% of the half-hourly mean $SWin_{Amola}$) to 176.14 W m^{-2} (96% of the half-hourly mean $SWin_{Amola}$) (Table 1). The modelled values are generally underestimated if compared to the measured ones. This can be due to cloudy conditions prevailing at the three off-glacier AWSs, which reduce the radiative input. Moreover, the multireflection from the snow-covered surfaces surrounding the glacier could increase $SWin_{Amola}$ values. Another factor leading to differences between $SWin_{Amola}$ and the modelled values obtained from the off-glacier AWSs is shading, both from topography and from cast shadow on the radiation sensors from the other sensors on the AWSs; concerning topographic shading, uncertainties can arise from the shading model used. In fact, in order to find the highest obstructing peak along the grid-point-to-the-Sun direction for each half-hour of the day, we set a grid step of 30 m. Probably choosing a lower grid step would produce a more reliable model.

Slightly better results were observed considering a daily time resolution: errors range from 30.92 W m^{-2} (17% of the daily mean $SWin_{Amola}$) to 68.13 W m^{-2} (38% of the daily mean $SWin_{Amola}$) (Table 2). These results suggest an extreme variability in hourly meteorological conditions among the sites and that no station is able to represent the same atmospheric absorption occurring over the Amola Glacier. Therefore, we decided to consider the SWin measured directly by the AWS_{Amola} in order to model the SWin distributed over the whole glacier surface. This assumption was applied by Senese et al. (2016) as well.

Although none of the three stations is able to accurately represent $SWin_{Amola}$, it is still possible to estimate T_s using daily SWin from the off-glacier stations and the empirical formula in Eq. (5); we therefore calculated T_s and subsequently buried ice ablation from modelled daily $SWin_{Caret}$, $SWin_{Pinzolo}$ and $SWin_{Presena}$. Similar melt amounts were found compared to $SWin_{Amola}$; In fact, using SWin from $AWS_{Presena}$ actually results in a slightly lower RMSE (0.15 m compared to 0.16 m for AWS_{Amola}) if compared with observed melt at the stakes between 21 July and 18 August 2020, whereas a worse RMSE was found for the other stations, with the worst results for Caret (see Table 3). However, all off-glacier AWSs show a similar or worse MAE and a worse bias in modelling melt in comparison with AWS_{Amola}, with the worst result again obtained for Caret station (0.07 m).

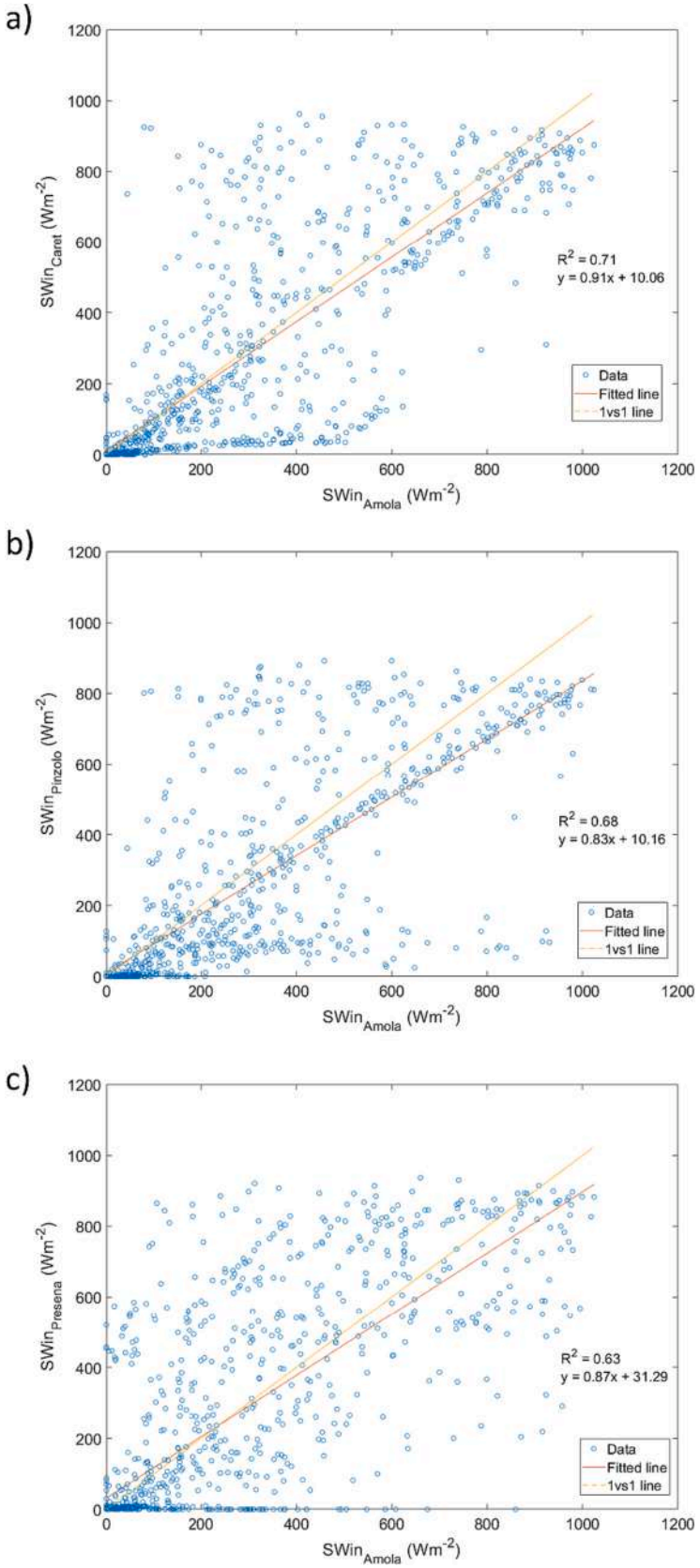

Fig. 7. Comparison between the incoming solar radiation measured by AWS_{Amola} ($SWin_{Amola}$) and the modelled values using data acquired by the automatic weather stations at A) Malga Caret ($SWin_{Caret}$), B) Pinzolo ($SWin_{Pinzolo}$) and C) Cima Presena ($SWin_{Presena}$). Data are half-hourly averages from 21 July to 18 August 2020.

Table 2
Comparison between the incoming solar radiation measured by AWS_{amola} and the modelled values using data acquired by the automatic weather stations at Malga Caret ($SWin_{Caret}$), Pinzolo ($SWin_{Pinzolo}$) and Cima Presena ($SWin_{Presena}$). The Root Mean Square Error (RMSE) between modelled and measured values is shown.

	Half-hourly					Daily		
	RMSE (W m^{-2})	%	r	Measured-Modelled >30 W m^{-2}	Measured-Modelled <−30 W m^{-2}	RMSE (W m^{-2})	%	r
$SWin_{Caret}$	153.46	84%	0.84	27%	15%	30.92	17%	0.92
$SWin_{Pinzolo}$	156.02	85%	0.83	34%	12%	43.29	24%	0.87
$SWin_{Presena}$	176.14	96%	0.80	25%	20%	68.13	38%	0.77

Table 3
Comparison between melt modelled using off-glacier incoming shortwave radiation from three Automatic Weather Stations (AWS) and the observed melt at the stakes between 21 July and 18 August 2020. Statistics include the Mean Absolute Error (MAE), Mean Bias Error (MBE) and Root Mean Square Error (RMSE).

Off-glacier AWS	MAE (m)	MBE (m)	RMSE (m)
Caret	0.12	0.07	0.18
Pinzolo	0.12	0.05	0.17
Cima Presena	0.14	−0.05	0.15

5.2. Modelling debris thickness from different satellite images

We checked the consistency of the DT - T_s relationship by using a Landsat 8 TIRS image outside of the observation period of AWS_{Amola}. We used the image acquired on 20 September 2020 for this purpose; the image was processed in the same way as the one from 28 July. The relationship between Landsat-derived T_s and DT was estimated with an exponential fit, with an R^2 of 0.63, slightly lower than using the image from 28 July (0.65). Landsat-derived T_s was generally lower on that day on the glacier at the time of image acquisition, with an average of 5.43 °C compared to 7.27 °C, compared to the image from 28 July. However, the relationship predicts larger debris thickness, with a maximum of 0.70 m and an average of 0.11 m, compared to 0.25 m and 0.08 m, respectively. At AWS_{Amola}, the calculated DT in this case is 0.07 m, compared to a measured value of 0.05 m.

When using DT modelled from the Landsat 8 TIRS image acquired on 20 September, very small differences can be observed in modelled melt compared to the image from 28 July. All the statistics considered are the same, with a RMSE of 0.16, a MAE of 0.12 and bias of −0.03. This suggests that debris cover at the site is relatively stable and that using thermal images acquired up to one month outside of the field season does not produce further uncertainty when modelling sub-debris melt.

5.3. Model uncertainties and possible improvements

The comparison between the empirical melt model and measurements from ablation stakes highlighted some discrepancies between modelled and measured melt; the RMSE of 22% is comparable to several other empirical models for ice-free and debris-covered ice; in Karakorum, a RMSE of 17% of cumulated melt was found by Minora et al. (2015) for debris-covered ice; in the Alps, Senese et al. (2021) found errors of 12–33% when comparing a set of empirical models with the full energy balance for debris-free ice on Forni Glacier. We identified several sources of uncertainty that can contribute to our RMSE. Among them, the spatial scale has probably a large influence, owing to the small size of Amola glacier (0.68 km^2) and the spatial resolution of modelled incoming shortwave radiation (30 m) and thermal data (100 m from Landsat 8 OLI, interpolated to 30 m), which might not accurately represent local conditions. While modelling shortwave radiation at a higher spatial scale is complicated by the availability of high resolution digital elevation models and the high computing requirements necessary to calculate shading, higher resolution thermal data compared to Landsat 8 OLI might be acquired from UAVs, as done by Kraaijenbrink et al. (2018) or a thermal camera in a fixed position, as in the study of Tarca and Guglielmin (2022).

Beside modelled quantities, other sources of uncertainty are related to the measured data as well. Specifically, data gaps occurred in the meteorological record from AWS_{Amola}, and gap-filling of SWin was necessary to estimate daily T_s and melt. In view of the power consumption of the sensors and cloud cover at the site, higher wattage solar panels (40 W or higher) and lead-gel batteries would be required to provide an uninterrupted data record, as discussed in Senese et al. (2018b). Measured ablation and debris thickness are also affected by uncertainties often difficult to quantify. In addition, they are point measurements and might not accurately estimate mass loss in an area of 30 m as used in the model, as differences of several tens of centimetres can easily develop during the ablation season between point measurements and nearby areas (Müller and Keeler, 1969). The same issue also affects temperature as measured from thermistor probes, which besides their inherent accuracy can undergo malfunctioning, as occurred in our case for the thermistor T5. To evaluate the potential of determining thermistor temperatures in case of malfunctioning, we compared T_s at the AWS_{Amola} against temperatures derived from LWout and observed a high correlation coefficient (0.85). The relationship between the two variables is rather good for lower (< 10 °C) and nighttime temperatures but the spread increases for higher ones, and temperature from LWout is overestimated compared to the one measured by the thermistor (see Fig. 8), which was placed under a rock. A similar result was observed by Brock et al. (2010) for thermistors placed at 2–3 cm depth, and is probably related to the steep thermal gradients in the first few cm of debris (see also Fig. 5). In addition, since the net radiometer is installed at a height of about 2 m, we can assume a contribution from the warm air layer between the surface and the sensor with a consequently overestimated measured LWout (Senese et al., 2012).

In our model, we assumed a linear gradient of debris temperature with depth, and demonstrated that the assumption holds true for the daily scale (see Fig. 5), but it is not verified for sub-daily time periods. This is in agreement with Nicholson and Benn (Nicholson and Benn, 2013; Nicholson and Benn, 2006), who demonstrated this behaviour for debris of different lithology and grain size. To compute melt at an hourly scale, a different approach would therefore be needed. Most studies have done so by solving the energy balance at the debris surface using satellite surface temperature to derive DT, with meteorological data from an AWS as input (Foster et al., 2012; Rounce and McKinney, 2014). This approach however relies on the calculation of all energy fluxes at the surface and debris-ice interface including turbulent fluxes, which require a wind and pressure sensor not deployed on AWS_{Amola}, as well as the extrapolation of these fluxes from the AWS to the entire glacier surface, with uncertainties related to the distribution of air temperature as well as the estimation of surface roughness (Foster et al., 2012). However, the method might have the potential to be employed without field- and time-dependent calibration, used in the empirical approach, if meteorological parameters are acquired from reanalysis products (Schauwecker et al., 2015). Other approaches which are first calibrated using the glacier energy balance include a debris-enhanced T-Index model developed by Carenzo et al. (2016), which is based on the calculation of cumulated air temperature and shortwave radiation, and requires empirical coefficients for both as well as lag coefficients accounting for the delaying effect introduced by debris. Such a model might also be tested on AWS_{Amola}, although spatially distributing melt

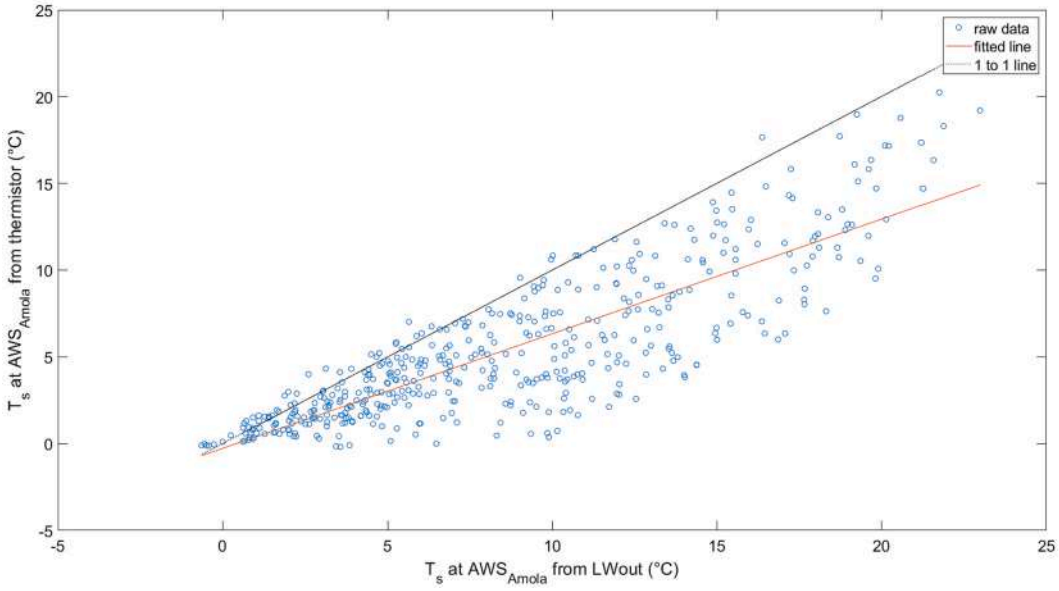

Fig. 8. Comparison between surface temperature (T_s) modelled from outgoing longwave radiation (LWout) and measured by the thermistor at AWS_{Amola} between 21 July 2020 and 18 August 2020.

would also require the extrapolation of air temperature on the glacier surface.

Recent studies have adopted another methodology to derive debris thickness, by fitting the Østrem curve (Østrem, 1959), relating debris thickness and melt to sub-debris ice melt in energy balance simulations for varying debris thickness and then using it to estimate spatially distributed debris thickness from distributed melt. The latter is obtained from geodetic mass balance (Ragettli et al., 2015), potentially corrected for the ice flux divergence (Rounce et al., 2018). The advantage of this approach is that it does not require thermal data, which is limited by the coarse resolution of satellite sensors (100 m interpolated for Landsat 8/9 OLI and 90 m for ASTER TIRS) or the difficulties in undertaking and processing data from thermal surveys from UAVs or field-based cameras. Therefore, it has great potential to produce accurate estimates of debris thickness. Nevertheless, local calibration of the Østrem curve for the conditions at Amola glacier would be required, as well as a geodetic mass balance, ideally from high-resolution DEMs.

Finally, a global map of glacier debris thickness estimated using a sub-debris melt-inversion and temperature-inversion approach is available from Rounce et al. (2021); the maximum debris thickness modelled for Amola glacier is 0.16 m, which clearly underestimates ground observations, and does not capture the patterns observed in Fig. 6 with our empirical approach; however, the approach uses calibration coefficients for the melt- and temperature-inversion from other nearby glaciers which might not be appropriate for Amola glacier.

6. Conclusions

In this study, we investigated meteorological and thermal conditions of a small debris-covered glacier of the Italian Alps, Amola glacier, and used an empirical model to estimate debris-covered ice melt over the course of a month during the ablation season 2020. The model is based on incoming shortwave radiation, surface temperature, thickness and thermal resistance of the debris layer, assuming a linear temperature gradient within the debris mantle. Incoming shortwave radiation was obtained by estimating exoatmospheric radiation from a modelling approach and correcting it for local cloud conditions using observations from an automatic weather station; surface temperature was derived assuming a linear relationship with shortwave radiation and debris thickness; the latter was spatially extrapolated using satellite temperatures from Landsat 8 OLI while thermal resistance was calculated through a network of ablation stakes.

The model is able to capture debris thickness, surface temperature and melt patterns of Amola glacier, including the increase in debris thickness close to the terminus and the left flank of the glacier, with consequent lower melt, and the decreasing debris thickness with elevation, which leads to higher melt in the upper parts of the continuous debris mantle. Modelled melt ranges between approximately 0.30 m and >1.50 m over approximately a month, with an RMSE of 0.16 m compared to ground observations from 9 ablation stakes, corresponding to 22% of average observed melt.

We also tested varying inputs to the melt model, by using off-glacier weather stations to correct modelled exoatmospheric radiation and a thermal image acquired 1 month apart from field observations to model debris thickness. Observations from off-glacier automatic weather stations are unable to capture the local solar radiation receipts of Amola glacier, with an RMSE of 17–34% of daily incoming radiation. However, since the model empirically relates solar radiation to surface temperature in melt calculation, the stations can still be used for melt modelling without compromising the accuracy. Similarly, using a thermal satellite image acquired 1 month apart does not result in a higher RMSE of modelled melt, which suggests a relative stability of the debris mantle during the ablation season.

Alternative approaches might be tested to improve the estimates of meltwater production of Amola glacier, based on solving the energy balance; however, the approaches rely on a full set of meteorological parameters to be acquired, and a comparison with off-glacier AWSs should also be performed to investigate whether the latter can be used to infer meteorological fluxes on the glacier surface.

In summary, our study provides an estimate of buried ice melt using a simple empirical model with a small number of meteorological and glaciological parameters obtained on the field. The performance of the model is comparable with that of empirical models used for debris-free and debris-covered ice in other glaciated regions. In view of the increasing importance of debris-covered glaciers for the hydrology of high mountain catchments, and of the logistic difficulties of installing and maintaining on-glacier automatic weather stations measuring a full set of parameters to derive the glacier energy balance, the empirical model could be used to provide an estimate of buried ice melt in the whole Adamello region. Further research is needed to extend the

applicability of the empirical model in time and space.

Funding

This research was funded by Levissima Sanpellegrino S.p.A., ECOFIBRE s.r.l., EDILFLOOR S.p.A., Geo&tex 2000 S.p.A. and Manifattura Fontana S.p.A and was supported by AssINGeo – Associazione Imprese Nazionali Geosintetici.

CRediT authorship contribution statement

D. Fugazza: Conceptualization, Methodology, Software, Formal analysis, Investigation, Data curation, Writing – original draft. **B. Valle:** Formal analysis, Investigation, Writing – original draft. **M. Caccianiga:** Investigation, Writing – original draft. **M. Gobbi:** Investigation, Writing – original draft. **G. Traversa:** Investigation, Writing – original draft. **M. Tognetti:** Investigation, Writing – original draft. **G.A. Diolaiuti:** Writing – original draft, Project administration, Funding acquisition. **A. Senese:** Conceptualization, Methodology, Formal analysis, Data curation, Writing – original draft, Supervision, Funding acquisition.

Declaration of Competing Interest

The authors declare that they have no known competing financial interests or personal relationships that could have appeared to influence the work reported in this paper.

Data availability

Landsat 8 OLI data are available from Earth Explorer at https://earthexplorer.usgs.gov/; weather station data from Meteo Trentino are available from https://www.meteotrentino.it/#!/content?menuItemDesktop=111. Data from the AWS_{Amola}, ablation stakes and thermistors are available upon request to the corresponding author.

Acknowledgments

We thank Levissima Sanpellegrino S.p.A, ECOFIBRE s.r.l., EDILFLOOR S.p.A., Geo&tex 2000 S.p.A. and Manifattura Fontana S.p.A and AssINGeo – Associazione Imprese Nazionali Geosintetici for their support. We acknowledge the park authority of Adamello Brenta National Park for authorizing the research activities, MTX for lending components of the AWS, Rifugio Segantini for the logistic support and Diego Maroni for helping with field data collection.

Appendix A. Supplementary data

Supplementary data to this article can be found online at https://doi.org/10.1016/j.coldregions.2023.104008.

References

Anderson, L.S., Anderson, R.S., 2016. Modeling debris-covered glaciers: response to steady debris deposition. Cryosphere 10, 1105–1124. https://doi.org/10.5194/tc-10-1105-2016.

Anslow, F.S., Hostetler, S., Bidlake, W.R., Clark, P.U., 2008. Distributed energy balance modeling of South Cascade Glacier, Washington and assessment of model uncertainty. J. Geophys. Res. Earth 113. https://doi.org/10.1029/2007JF000850.

Azzoni, R.S., Senese, A., Zerboni, A., Maugeri, M., Smiraglia, C., Diolaiuti, G.A., 2016. Estimating ice albedo from fine debris cover quantified by a semi-automatic method: the case study of Forni Glacier, Italian Alps. Cryosphere 10, 665–679. https://doi.org/10.5194/tc-10-665-2016.

Azzoni, R.S., Fugazza, D., Zerboni, A., Senese, A., D'Agata, C., Maragno, D., Carzaniga, A., Cernuschi, M., Diolaiuti, G.A., 2018. Evaluating high-resolution remote sensing data for reconstructing the recent evolution of supra glacial debris: a study in the Central Alps (Stelvio Park, Italy). Progr. Phys. Geogr. Earth Environ. 42, 3–23. https://doi.org/10.1177/0309133317749434.

Barnett, T.P., Adam, J.C., Lettenmaier, D.P., 2005. Potential impacts of a warming climate on water availability in snow-dominated regions. Nature 438, 303–309. https://doi.org/10.1038/nature04141.

Baroni, C., Carton, A., Seppi, R., 2004. Distribution and behaviour of rock glaciers in the Adamello–Presanella Massif (Italian Alps). Permafr. Periglac. Process. 15, 243–259. https://doi.org/10.1002/ppp.497.

Belloni, S., Pelfini, M., 1995. Glaciers as climatic indicators. Geogr. Fis. Din. Quat. 18, 185–189.

Beniston, M., Keller, F., Goyette, S., 2003. Snow pack in the Swiss Alps under changing climatic conditions: an empirical approach for climate impacts studies. Theor. Appl. Climatol. 74, 19–31.

Benn, D., Evans, D.J.A., 2010. Glaciers and Glaciation, 2nd Edition. Routledge, London.

Benn, D.I., Kirkbride, M.P., Owen, L.A., Brazier, V., 2014. Glaciated valley landsystems. In: Gooster, L., Evans, D. (Eds.), Glacial Landsystems. Taylor & Francis, pp. 372–406. https://doi.org/10.4324/9780203784976.

Bocchiola, D., Diolaiuti, G., 2010. Evidence of climate change within the Adamello Glacier of Italy. Theor. Appl. Climatol. 100, 351–369. https://doi.org/10.1007/s00704-009-0186-x.

Bocchiola, D., Senese, A., Mihalcea, C., Mosconi, B., D'Agata, C., Smiraglia, C., Diolaiuti, G.A., 2015. An ablation model for debris-covered ice: the case study of Venerocolo glacier (Italian Alps). Geogr. Fis. Din. Quat. 113–128 https://doi.org/10.4461/GFDQ.2015.38.11.

Bocchiola, D., Soncini, A., Senese, A., Diolaiuti, G., 2018. Modelling hydrological components of the Rio Maipo of Chile, and their prospective evolution under climate change. Climate 6, 57. https://doi.org/10.3390/cli6030057.

Brock, B.W., Mihalcea, C., Kirkbride, M.P., Diolaiuti, G., Cutler, M.E.J., Smiraglia, C., 2010. Meteorology and surface energy fluxes in the 2005–2007 ablation seasons at the Miage debris-covered glacier, Mont Blanc Massif, Italian Alps. J. Geophys. Res. Atmos. 115 https://doi.org/10.1029/2009JD013224.

Caccianiga, M., Andreis, C., Diolaiuti, G., D'Agata, C., Mihalcea, C., Smiraglia, C., 2011. Alpine debris-covered glaciers as a habitat for plant life. The Holocene. https://doi.org/10.1177/0959683611400219.

Carenzo, M., Pellicciotti, F., Mabillard, J., Reid, T., Brock, B.W., 2016. An enhanced temperature index model for debris-covered glaciers accounting for thickness effect. Adv. Water Resour. 94, 457–469. https://doi.org/10.1016/j.advwatres.2016.05.001.

Chesnokova, A., Baraër, M., Laperrière-Robillard, T., Huh, K., 2020. Linking Mountain Glacier retreat and hydrological changes in Southwestern Yukon. Water Resour. Res. 56, e2019WR025706 https://doi.org/10.1029/2019WR025706.

Foster, L.A., Brock, B.W., Cutler, M.E.J., Diotri, F., 2012. A physically based method for estimating supraglacial debris thickness from thermal band remote-sensing data. J. Glaciol. 58, 677–691. https://doi.org/10.3189/2012JoG11J194.

Franzetti, A., Navarra, F., Tagliaferri, I., Gandolfi, I., Bestetti, G., Minora, U., Azzoni, R. S., Diolaiuti, G., Smiraglia, C., Ambrosini, R., 2017. Potential sources of bacteria colonizing the cryoconite of an Alpine glacier. PLoS One 12, e0174786. https://doi.org/10.1371/journal.pone.0174786.

Fujita, K., Sakai, A., 2014. Modelling runoff from a Himalayan debris-covered glacier. Hydrol. Earth Syst. Sci. 18, 2679–2694. https://doi.org/10.5194/hess-18-2679-2014.

Fyffe, C.L., Reid, T.D., Brock, B.W., Kirkbride, M.P., Diolaiuti, G., Smiraglia, C., Diotri, F., 2014. A distributed energy-balance melt model of an alpine debris-covered glacier. J. Glaciol. 60, 587–602. https://doi.org/10.3189/2014JoG13J148.

Gibson, M.J., Irvine-Fynn, T.D.L., Wagnon, P., Rowan, A.V., Quincey, D.J., Homer, R., Glasser, N.F., 2018. Variations in near-surface debris temperature through the summer monsoon on Khumbu Glacier, Nepal Himalaya. Earth Surf. Process. Landf. 43, 2698–2714. https://doi.org/10.1002/esp.4425.

Gjermundsen, E.F., Mathieu, R., Kääb, A., Chinn, T., Fitzharris, B., Hagen, J.O., 2011. Assessment of multispectral glacier mapping methods and derivation of glacier area changes, 1978–2002, in the central Southern Alps, New Zealand, from ASTER satellite data, field survey and existing inventory data. J. Glaciol. 57, 667–683. https://doi.org/10.3189/002214311797409749.

Gobbi, M., Ballarin, F., Brambilla, M., Composla, C., Isaia, M., Losapio, G., Maffioletti, C., Seppi, R., Tampucci, D., Caccianiga, M., 2017. Life in harsh environments: carabid and spider trait types and functional diversity on a debris-covered glacier and along its foreland. Ecol. Entomol. 42, 838–848. https://doi.org/10.1111/een.12456.

Guglielmin, M., 2006. Ground surface temperature (GST), active layer and permafrost monitoring in continental Antarctica. Permafr. Periglac. Process. 17, 133–143.

Guglielmin, M., Ellis-Evans, C.J., Cannone, N., 2008. Active layer thermal regime under different vegetation conditions in permafrost areas. A case study at Signy Island (Maritime Antarctica). Geoderma 144, 73–85. https://doi.org/10.1016/j.geoderma.2007.10.010.

Han, H., Ding, Y., Liu, S., 2006. A simple model to estimate ice ablation under a thick debris layer. J. Glaciol. 52, 528–536. https://doi.org/10.3189/172756506781828395.

Hartmann, D.L., 2015. Global Physical Climatology, 2° edizione. ed. Elsevier Science, Amsterdam, Boston.

Huss, M., Hock, R., 2018. Global-scale hydrological response to future glacier mass loss. Nat. Clim. Chang. 8, 135–140. https://doi.org/10.1038/s41558-017-0049-x.

Huss, M., Bookhagen, B., Huggel, C., Jacobsen, D., Bradley, R.S., Clague, J.J., Vuille, M., Buytaert, W., Cayan, D.R., Greenwood, G., Mark, B.G., Milner, A.M., Weingartner, R., Winder, M., 2017. Toward mountains without permanent snow and ice. Earth's Future 5, 418–435. https://doi.org/10.1002/2016EF000514.

Kaser, G., Fountin, A., Jansson, P., 2003. A Manual for Monitoring the Mass Balance of Mountain Glaciers (IHP VI - Technical Documents in Hydrology No. 59). UNESCO-IHP, Paris.

Kirkbride, M.P., 2011. Debris-covered glaciers. In: Singh, V.P., Singh, P., Haritashya, U. K. (Eds.), Encyclopedia of Snow, Ice and Glaciers, Encyclopedia of Earth Sciences. Springer, pp. 190–192. https://doi.org/10.1007/978-90-481-2642-2.

Kirkbride, M.P., Deline, P., 2013. The formation of supraglacial debris covers by primary dispersal from transverse englacial debris bands. Earth Surf. Process. Landf. 38, 1779–1792. https://doi.org/10.1002/esp.3416.
Konzelmann, T., Ohmura, A., 1995. Radiative fluxes and their impact on the energy balance of the Greenland ice sheet. J. Glaciol. 41, 490–502. https://doi.org/10.3189/S0022143000034833.
Kraaijenbrink, P.D.A., Bierkens, M.F.P., Lutz, A.F., Immerzeel, W.W., 2017. Impact of a global temperature rise of 1.5 degrees Celsius on Asia's glaciers. Nature 549, 257–260. https://doi.org/10.1038/nature23878.
Kraaijenbrink, P.D.A., Shea, J.M., Litt, M., Steiner, J.F., Treichler, D., Koch, I., Immerzeel, W.W., 2018. Mapping surface temperatures on a Debris-Covered glacier with an unmanned aerial vehicle. Front. Earth Sci. 6.
Losapio, G., Jordán, F., Caccianiga, M., Gobbi, M., 2015. Structure-dynamic relationship of plant–insect networks along a primary succession gradient on a glacier foreland. Ecol. Model. 314, 73–79. https://doi.org/10.1016/j.ecolmodel.2015.07.014.
Maragno, D., Diolaiuti, G., D'Agata, C., Mihalcea, C., Bocchiola, D., Janetti, E.B., Riccardi, A., Smiraglia, C., 2009. New evidence from Italy (Adamello group, Lombardy) for analysing the ongoing decline of Alpine glaciers. Geogr. Fis. Din. Quat. 32, 31–39.
Marzeion, B., Champollion, N., Haeberli, W., Langley, K., Leclercq, P., Paul, F., 2017. Observation-based estimates of global glacier mass change and its contribution to sea-level change. Surv. Geophys. 38, 105–130. https://doi.org/10.1007/s10712-016-9394-y.
Mattson, L.E., Gardner, J.S., Young, G.J., 1993. Ablation on Debris covered Glaciers: an example from the Rakhiot Glacier, Punjab, Himalaya. Present. Snow Glacier Hydrol. 289–296.
Mihalcea, C., Brock, B.W., Diolaiuti, G., D'Agata, C., Citterio, M., Kirkbride, M.P., Cutler, M.E.J., Smiraglia, C., 2008a. Using ASTER satellite and ground-based surface temperature measurements to derive supraglacial debris cover and thickness patterns on Miage Glacier (Mont Blanc Massif, Italy). Cold Reg. Sci. Technol. 52, 341–354. https://doi.org/10.1016/j.coldregions.2007.03.004.
Mihalcea, C., Mayer, C., Diolaiuti, G., D'Agata, C., Smiraglia, C., Lambrecht, A., Vuillermoz, E., Tartari, G., 2008b. Spatial distribution of debris thickness and melting from remote-sensing and meteorological data, at debris-covered Baltoro glacier, Karakoram, Pakistan. Ann. Glaciol. 48, 49–57. https://doi.org/10.3189/172756408784700680.
Minora, U., Senese, A., Bocchiola, D., Soncini, A., D'agata, C., Ambrosini, R., Mayer, C., Lambrecht, A., Vuillermoz, E., Smiraglia, C., Diolaiuti, G., 2015. A simple model to evaluate ice melt over the ablation area of glaciers in the Central Karakoram National Park, Pakistan. Ann. Glaciol. 56, 202–216. https://doi.org/10.3189/2015AoG70A206.
Müller, F., Keeler, C.M., 1969. Errors in short-term ablation measurements on melting ice surfaces. J. Glaciol. 8, 91–105. https://doi.org/10.3189/S0022143000020785.
Nakawo, M., Rana, B., 1999. Estimate of ablation rate of glacier ice under a supraglacial debris layer. Geogr. Ann. Ser. B 81, 695–701. https://doi.org/10.1111/1468-0459.00097.
Nakawo, M., Young, G.J., 1981. Field experiments to determine the effect of a Debris Layer on ablation of glacier ice. Ann. Glaciol. 2, 85–91. https://doi.org/10.3189/172756481794352432.
Nicholson, L., Benn, D.I., 2006. Calculating ice melt beneath a debris layer using meteorological data. J. Glaciol. 52, 463–470. https://doi.org/10.3189/172756506781828584.
Nicholson, L., Benn, D.I., 2013. Properties of natural supraglacial debris in relation to modelling sub-debris ice ablation. Earth Surf. Process. Landf. 38, 490–501. https://doi.org/10.1002/esp.3299.
Osterkamp, T.E., 2003. Establishing long-term permafrost observatories for active-layer and permafrost investigations in Alaska: 1977–2002. Permafr. Periglac. Process. 14, 331–342. https://doi.org/10.1002/ppp.464.
Østrem, G., 1959. Ice Melting under a Thin Layer of Moraine, and the Existence of Ice Cores in Moraine Ridges. Geogr. Ann. 41, 228–230. https://doi.org/10.1080/20014422.1959.11907953.
Paul, F., Kääb, A., Haeberli, W., 2007. Recent glacier changes in the Alps observed by satellite: consequences for future monitoring strategies. In: Global and Planetary Change, Climate Change Impacts on Mountain Glaciers and Permafrost, 56, pp. 111–122. https://doi.org/10.1016/j.gloplacha.2006.07.007.
Paul, F., Rastner, P., Azzoni, R.S., Diolaiuti, G., Fugazza, D., Le Bris, R., Nemec, J., Rabatel, A., Ramusovic, M., Schwaizer, G., Smiraglia, C., 2020. Glacier shrinkage in the Alps continues unabated as revealed by a new glacier inventory from Sentinel-2. Earth Syst. Sci. Data 12, 1805–1821. https://doi.org/10.5194/essd-12-1805-2020.
Ragettli, S., Pellicciotti, F., Immerzeel, W.W., Miles, E.S., Petersen, L., Heynen, M., Shea, J.M., Stumm, D., Joshi, S., Shrestha, A., 2015. Unraveling the hydrology of a Himalayan catchment through integration of high resolution in situ data and remote sensing with an advanced simulation model. Adv. Water Resour. 78, 94–111. https://doi.org/10.1016/j.advwatres.2015.01.013.
Reid, T.D., Brock, B.W., 2010. An energy-balance model for debris-covered glaciers including heat conduction through the debris layer. J. Glaciol. 56, 903–916. https://doi.org/10.3189/002214310794457218.
Roe, G.H., Baker, M.B., Herla, F., 2017. Centennial glacier retreat as categorical evidence of regional climate change. Nat. Geosci. 10, 95–99. https://doi.org/10.1038/ngeo2863.
Rounce, D.R., McKinney, D.C., 2014. Debris thickness of glaciers in the Everest area (Nepal Himalaya) derived from satellite imagery using a nonlinear energy balance model. Cryosphere 8, 1317–1329. https://doi.org/10.5194/tc-8-1317-2014.
Rounce, D.R., Quincey, D.J., McKinney, D.C., 2015. Debris-covered glacier energy balance model for Imja–Lhotse Shar Glacier in the Everest region of Nepal. Cryosphere 9, 2295–2310. https://doi.org/10.5194/tc-9-2295-2015.
Rounce, D.R., King, O., McCarthy, M., Shean, D.E., Salerno, F., 2018. Quantifying Debris thickness of debris-covered glaciers in the everest region of Nepal through inversion of a subdebris melt model. J. Geophys. Res. Earth 123, 1094–1115. https://doi.org/10.1029/2017JF004395.
Rounce, D.R., Hock, R., McNabb, R.W., Millan, R., Sommer, C., Braun, M.H., Malz, P., Maussion, F., Mouginot, J., Seehaus, T.C., Shean, D.E., 2021. Distributed Global Debris thickness estimates reveal Debris significantly impacts glacier mass balance. Geophys. Res. Lett. 48, e2020GL091311 https://doi.org/10.1029/2020GL091311.
Rozenstein, O., Qin, Z., Derimian, Y., Karnieli, A., 2014. Derivation of land surface temperature for Landsat-8 TIRS using a split window algorithm. Sensors 14, 5768–5780. https://doi.org/10.3390/s140405768.
Schauwecker, S., Rohrer, M., Huggel, C., Kulkarni, A., Ramanathan, A., Salzmann, N., Stoffel, M., Brock, B., 2015. Remotely sensed debris thickness mapping of Bara Shigri Glacier, Indian Himalaya. J. Glaciol. 61, 675–688. https://doi.org/10.3189/2015JoG14J102.
Senese, A., Diolaiuti, G., Mihalcea, C., Smiraglia, C., 2012. Energy and mass balance of Forni Glacier (Stelvio National Park, Italian Alps) from a four-year meteorological data record. Arct. Antarct. Alp. Res. 44, 122–134. https://doi.org/10.1657/1938-4246-44.1.122.
Senese, A., Maugeri, M., Ferrari, S., Confortola, G., Soncini, A., Bocchiola, D., Diolaiuti, G.A., 2016. Modelling shortwave and longwave downward radiation and air temperature driving ablation at the Forni glacier (Stelvio National Park, Italy). Geogr. Fis. Din. Quat. 39, 89–100.
Senese, A., Maragno, D., Fugazza, D., Soncini, A., D'Agata, C., Azzoni, R.S., Minora, U., Ul-Hassan, R., Vuillermoz, E., Khan, M.A., Rana, A.S., Rasul, G., Smiraglia, C., Diolaiuti, G.A., 2018a. Inventory of glaciers and glacial lakes of the Central Karakoram National Park (CKNP – Pakistan). J. Maps 14, 189–198. https://doi.org/10.1080/17445647.2018.1445561.
Senese, A., Maugeri, M., Meraldi, E., Verza, G.P., Azzoni, R.S., Compostella, C., Diolaiuti, G., 2018b. Estimating the snow water equivalent on a glacierized high elevation site (Forni Glacier, Italy). Cryosphere 12, 1293–1306. https://doi.org/10.5194/tc-12-1293-2018.
Senese, A., Manara, V., Maugeri, M., Diolaiuti, G.A., 2020. Comparing measured incoming shortwave and longwave radiation on a glacier surface with estimated records from satellite and off-glacier observations: a case study for the Forni Glacier, Italy. Remote Sens. 12, 3719. https://doi.org/10.3390/rs12223719.
Senese, A., Leidi, M., Diolaiuti, G.A., 2021. A new enhanced temperature index model including net solar and infrared radiation. Geogr. Fis. Din. Quat. 44, 3–12.
Smiraglia, C., Azzoni, R.S., D'Agata, C., Maragno, D., Fugazza, D., Diolaiuti, G.A., 2015. The evolution of the Italian glaciers from the previous data base to the new Italian inventory. Preliminary considerations and results. Geogr. Fis. Din. Quat. 79–87 https://doi.org/10.4461/GFDQ.2015.38.08.
Soncini, A., Bocchiola, D., Confortola, G., Bianchi, A., Rosso, R., Mayer, C., Lambrecht, A., Palazzi, E., Smiraglia, C., Diolaiuti, G., 2015. Future hydrological Regimes in the Upper Indus Basin: a case study from a high-altitude Glacierized catchment. J. Hydrometeorol. 16, 306–326. https://doi.org/10.1175/JHM-D-14-0043.1.
Stefaniak, A.M., Robson, B.A., Cook, S.J., Clutterbuck, B., Midgley, N.G., Labadz, J.C., 2021. Mass balance and surface evolution of the debris-covered Miage Glacier, 1990–2018. Geomorphology 373, 107474. https://doi.org/10.1016/j.geomorph.2020.107474.
Tampucci, D., Citterio, C., Gobbi, M., Caccianiga, M., 2016. Vegetation outlines of a debris-covered glacier descending below the treeline. Plant Sociol. 45–54 https://doi.org/10.7338/pls2016531/03.
Tampucci, D., Azzoni, R.S., Boracchi, P., Citterio, C., Compostella, C., Diolaiuti, G., Isaia, M., Marano, G., Smiraglia, C., Gobbi, M., Caccianiga, M., 2017. Debris-covered glaciers as habitat for plant and arthropod species: environmental framework and colonization patterns. Ecol. Complex. 32, 42–52. https://doi.org/10.1016/j.ecocom.2017.09.004.
Tarca, G., Guglielmin, M., 2022. Using ground-based thermography to analyse surface temperature distribution and estimate debris thickness on Gran Zebrù glacier (Ortles-Cevedale, Italy). Cold Reg. Sci. Technol. 196, 103487 https://doi.org/10.1016/j.coldregions.2022.103487.
Tenan, S., Maffioletti, C., Caccianiga, M., Compostella, C., Seppi, R., Gobbi, M., 2016. Hierarchical models for describing space-for-time variations in insect population size and sex-ratio along a primary succession. Ecol. Model. 329, 18–28. https://doi.org/10.1016/j.ecolmodel.2016.02.006.
Valle, B., di Musciano, M., Gobbi, M., Bonelli, M., Colonnelli, E., Gardini, G., Migliorini, M., Pantini, P., Zanetti, A., Berrilli, E., Frattaroli, A.R., Fugazza, D., Invernizzi, A., Caccianiga, M., 2022. Biodiversity and ecology of plants and arthropods on the last preserved glacier of the Apennines mountain chain (Italy). The Holocene. https://doi.org/10.1177/09596836221096292, 09596836221096292.
Zhang, T., Stamnes, K., Bowling, S.A., 1996. Impact of clouds on surface radiative fluxes and snowmelt in the Arctic and Subarctic. J. Clim. 9, 2110–2123. https://doi.org/10.1175/1520-0442(1996)009<2110:IOCOSR>2.0.CO;2.
Zhang, Y., Fujita, K., Liu, S., Liu, Q., Nuimura, T., 2011. Distribution of debris thickness and its effect on ice melt at Hailuogou glacier, southeastern Tibetan Plateau, using in situ surveys and ASTER imagery. J. Glaciol. 57, 1147–1157. https://doi.org/10.3189/002214311798843331.